Journal of Alloys and Compounds 954 (2023) 170192

Contents lists available at ScienceDirect

Journal of Alloys and Compounds

journal homepage: www.elsevier.com/locate/jalcom

Spectroscopic characterization of Er^{3+}-doped CaF_2 nanoparticles: Luminescence concentration quenching, radiation trapping and transition probabilities

Eugenio Cantelar *, Ginés Lifante-Pedrola, Marta Quintanilla, Juan Antonio Sanz-García, Fernando Cussó

Departamento de Física de Materiales, C-04, Facultad de Ciencias, Universidad Autónoma de Madrid, 28049 Madrid, Spain

ARTICLE INFO

Article history:
Received 27 February 2023
Received in revised form 14 April 2023
Accepted 17 April 2023
Available online 18 April 2023

Keywords:
CaF_2 nanoparticles
Er^{3+}
Concentration quenching
Radiation trapping
Judd-Ofelt

ABSTRACT

Er^{3+}-doped CaF_2 nanoparticles (NPs) with variable dopant concentration were synthesized by a direct precipitation method. X-Ray Powder Diffraction, SEM and TEM were used to analize the crystalline structure and morphology. The spectroscopic characterization, as function of the Er^{3+} content, has been performed under CW and pulsed excitation. Under steady state conditions, it has been found that the intensity of the main emission bands is affected by luminescence quenching processes. The population dynamics, recorded under pulsed excitation, confirms not only the existence of quenching processes but also the occurrence of radiation trapping. The intrinsic transition probabilities of the main Er^{3+} emitting manifolds, in absence of quenching and radiation trapping, have been estimated through a procedure commonly used in bulk doped materials. A modified Judd-Ofelt analysis has been performed to determine the radiative transition probabilities, radiative lifetimes and branching ratios of the Er^{3+} levels. Finally, an estimation of the gap law in these NPs is given.

1. Introduction

At present, fluoride nanoparticles doped with trivalent lanthanide ions (Ln^{3+}) are arousing great interest in applications that demand efficient luminescent transitions and, therefore, high quantum efficiency values. Additionally, it is also common that the application needs of high emission intensities, only achievable if a large number of optical centers is available [1–3]. However, it is not easy to simultaneously satisfy both requirements and, in general, a compromise between quantum efficiency and high values of active ion densities must be sought.

The population dynamics in Ln^{3+}-doped nanoparticles (NPs), as well as in their bulk counterparts, is in general complex, being strongly dependent on the active ion concentration. Thus, while in diluted systems the population dynamics is governed by spontaneous relaxations (radiative and non-radiative transitions), in high concentrated systems the situation is clearly different. In fact, as the active ion concentration increases, the spontaneous transitions start to compete with ion-ion interactions such as energy migration and cross relaxation processes. These energy diffusion mechanisms give rise to an effective excitation of non-emitting centers (luminescent killers) that provoke to faster temporal decays and reduces the luminescent quantum efficiency.

These loss mechanisms, usually known as concentration quenching processes, are usually appreciable even under CW excitation conditions, since they give rise to a marked reduction in the total emission intensity [4–6]. However, they are more easily detectable in the temporal evolution of the luminescence since they provoke decays that are faster the higher the concentration of active ions [3,7].

Additionally, when lifetime measurements are performed, there is another important aspect that should be under consideration: the possibility of radiation trapping; that is, the reabsorption of the emitted radiation. Thus, at variance with the concentration quenching processes, the radiation trapping can affect the luminescent temporal decay even at low Ln^{3+} concentration, being particularly relevant when excited states are long living states [8,9].

Among the different fluoride compounds, CaF_2 has attracted attention due to its low phonon energy ($\hbar\Omega = 328cm^{-1}$ [10]) that ensures low non-radiative transition probabilities and, therefore, high luminescence quantum efficiencies. Additionally, like other alkali

* Correspondence to: Avda. Francisco Tomás y Valiente nº 7, Departamento de Física de Materiales, C-04, Facultad de Ciencias, Universidad Autónoma de Madrid, 28049 Madrid, Spain.
E-mail address: eugenio.cantelar@uam.es (E. Cantelar).

https://doi.org/10.1016/j.jallcom.2023.170192

earth fluorides, CaF_2 exhibits a broad range of solubility for Ln^{3+} ions. These trivalent ions are incorporated into the crystal lattice replacing the divalent Ca^{2+} ions giving rise to an excess of positive charge which is balanced by the incorporation of F^- ions in interstitial positions leading to several kinds of luminescent centers [11–14].

The fundamental electronic configuration of Er^{3+} ions, $[Xe]4f^{11}$, gives rise to a large number of fine structure levels providing, therefore, a wide variety of radiative transitions in the optical range. These transitions can be efficiently excited through different Stokes and/or anti-Stokes processes or even via energy transfer mechanisms from a different lanthanide ion, see for instance [15–19].

Although it is possible to find some works dealing about the synthesis and optical characterization of CaF_2:Er^{3+} NPs [20–23], the basic spectroscopic properties of these active ions in calcium fluoride nanostructures are not fully understood. In this work, CaF_2:Er^{3+} NPs with variable dopant concentration were synthesized by a direct precipitation method. X-Ray Powder Diffraction, SEM and TEM have been used to analyze the particle crystalline structure and morphology. The basic spectroscopy of Er^{3+} ions has been studied under CW and pulsed excitation as function of the dopant level. The dependence of the emission intensity of the main emission bands ($^2H_{11/2}$:$^4S_{3/2} \rightarrow {}^4I_{15/2}$, $^4F_{9/2} \rightarrow {}^4I_{15/2}$, $^2H_{11/2}$:$^4S_{3/2} \rightarrow {}^4I_{13/2}$, $^4I_{11/2} \rightarrow {}^4I_{15/2}$ and $^4I_{13/2} \rightarrow {}^4I_{15/2}$) reveals the presence of luminescence quenching processes that reduce the luminescence quantum efficiency as Er^{3+} concentration increases. The dynamics of the emitting manifolds, recorded under pulsed excitation, has confirmed the presence of these processes together with the existence of radiation trapping. A treatment, commonly used in bulk doped materials, has been applied to determine the intrinsic total transition probabilities of $^4I_{13/2}$, $^4I_{11/2}$, $^4F_{9/2}$ and $^2H_{11/2}$:$^4S_{3/2}$ erbium levels in absence of quenching and radiation trapping. The intrinsic total transition probability of $^4I_{13/2}$ level, has been used to perform a modified Judd-Ofelt analysis in order to determine the radiative transition probabilities, radiative lifetimes and branching ratios of Er^{3+} levels in the CaF_2 NPs. Finally, the non-radiative transition probabilities of $^4I_{11/2}$, $^4F_{9/2}$ and $^2H_{11/2}$:$^4S_{3/2}$ erbium levels, calculated from the intrinsic transition probabilities and the radiative ones, has allowed to determine the gap law in the CaF_2:Er^{3+} NPs.

2. Experimental details

2.1. Synthesis of nanoparticles

CaF_2:Er^{3+} NPs have been prepared following a direct chemical precipitation route, as described elsewhere [24–26]. The starting chemical reagents were $CaCl_2 \cdot 2\,H_2O$, $ErCl_3 \cdot 6\,H_2O$ and NH_4F all of them from Alfa Aesar with a purity level of 99.9%. This simple preparation method takes advantage of the high solubility in aqueous medium, and therefore, the high dissociation level, that possess calcium (or erbium) chlorides as well as ammonium fluoride to produce the Ca^{2+}, Er^{3+} and F^- ions whose chemical reaction gives rise to the precipitation of the Er^{3+}-doped CaF_2 NPs.

The concentration of the cationic precursors, in the form of $CaCl_2$ and $ErCl_3$ salts, were adjusted to synthesize NPs with variable erbium concentration, ranging from 0.7 mol% to 10 mol%. The salts were diluted in 200 mL of deionized water, taking care of the final solution concentration were 0.01 mol/l, and added to a beaker. The cationic solution was fixed to a pH value of 3 by adding 30 mg of hydrochloric acid (36%). Temperature was increased up to the boiling point (T = 100ºC) moment at which the anionic precursor, 0.08 mol/l solution of NH_4F, was slowly added to the beaker. The acid character of the cationic solution prevents the fast precipitation of the Er^{3+}-doped CaF_2 NPs. After the precipitation, the initial reagents were removed by centrifugation and the particles were washed with ethanol and deionized water. NPs were dried at 60 ºC during 24 h and then collected for subsequent characterization.

Table 1
Structural and morphological parameters of CaF_2:Er^{3+} NPs with different dopant levels.

Sample	[Er^{3+}] (mol%)	Lattice parameter $\boldsymbol{a} = \boldsymbol{b} = \boldsymbol{c}$ (Å)	Crystallite size (nm)	Mean particle size (nm)
# 0	0.0	5.4617	103	79 ± 39
# 1	0.7	5.4628	45	31 ± 13
# 2	1.3	5.4634	47	33 ± 11
# 3	2.4	5.4646	40	35 ± 15
# 4	3.8	5.4657	45	22 ± 15
# 5	5.5	5.4672	37	23 ± 16
# 6	6.5	5.4685	31	39 ± 13
# 7	10.0	5.4704	31	33 ± 15

2.2. Characterization techniques

X-Ray characterization techniques have been used to determine the erbium concentration and crystalline structure of the synthesized NPs. Erbium content in the nanoparticles was determined by X-Ray Fluorescence Spectrometry (TXRF), the corresponding values are presented in Table 1. Phase and crystalline structure were investigated by using an X'Pert Pro Theta/2Theta powder diffractometer (Cu K_α radiation, λ = 0.15406nm).

The size and morphology of the NPs were studied by a Philips XL30 S-FEG Scanning Electron Microscope (SEM) and a JEOL JEM-1400 Flash Transmission Electron Microscope (TEM) at CBM Severo Ochoa.

The spectroscopic characterization was performed by using several laser excitation sources. The emission spectra were measured under excitation at λ_{exc} = 488nm by using a CW Argon laser. It is important to remark that in order to compare the relative intensities of the different emission bands, the emission spectra shown in the following section were corrected taking into account the wavelength response of the measurement equipment.

The dynamics of the main emission bands was explored by using two different pumping schemes. In the first case, λ_{exc} = 532nm, excitation was achieved by using the second harmonic of a pulsed Nd:YAG laser (Spectra Pro model DCR2/2 A 3378 with a pulse width of 10 ns and a repetition rate of 10 Hz). In the second case, λ_{exc} = 650nm, excitation was made using a commercial diode laser electronically "modulated" by controlling the power injection with the help of an Arduino system, in order to obtain pulses with adjustable excitation and dark temporal windows. This scheme is particularly suitable to characterize decay signals having long decay times as it is the case for many of the erbium transitions in CaF_2. Independently on the excitation scheme, the luminescent signal was dispersed by using an ARC SpectraPro 500-i monochromator and detected with a photomultiplier or an InGaAs photodiode depending on the spectral range. Additionally, for lifetime measurements, a Tektronix DPO4104B-L digital oscilloscope was used to average synchronously the decay of the luminescent signals.

The absorption spectrum shown in the last section of this work was measured by using a Perkin Elmer Lambda 1050 spectrophotometer.

3. Results and discussion

3.1. Structural analysis

Fig. 1(a) shows the X-Ray Powder Diffraction (XRD) patterns of the CaF_2:Er^{3+} NPs as function of erbium concentration; the reported pattern of CaF_2 crystal (PDF 04–007–5933 from the International Centre of Diffraction Data, ICDD 2011) has been also included in the lower part of the figure. As it can be appreciated, the difraction peaks observed within the range 2θ = 20º to 2θ = 100º can be indexed to the fluoride-type structure ($Fm\bar{3}m$ space group), being associated to the

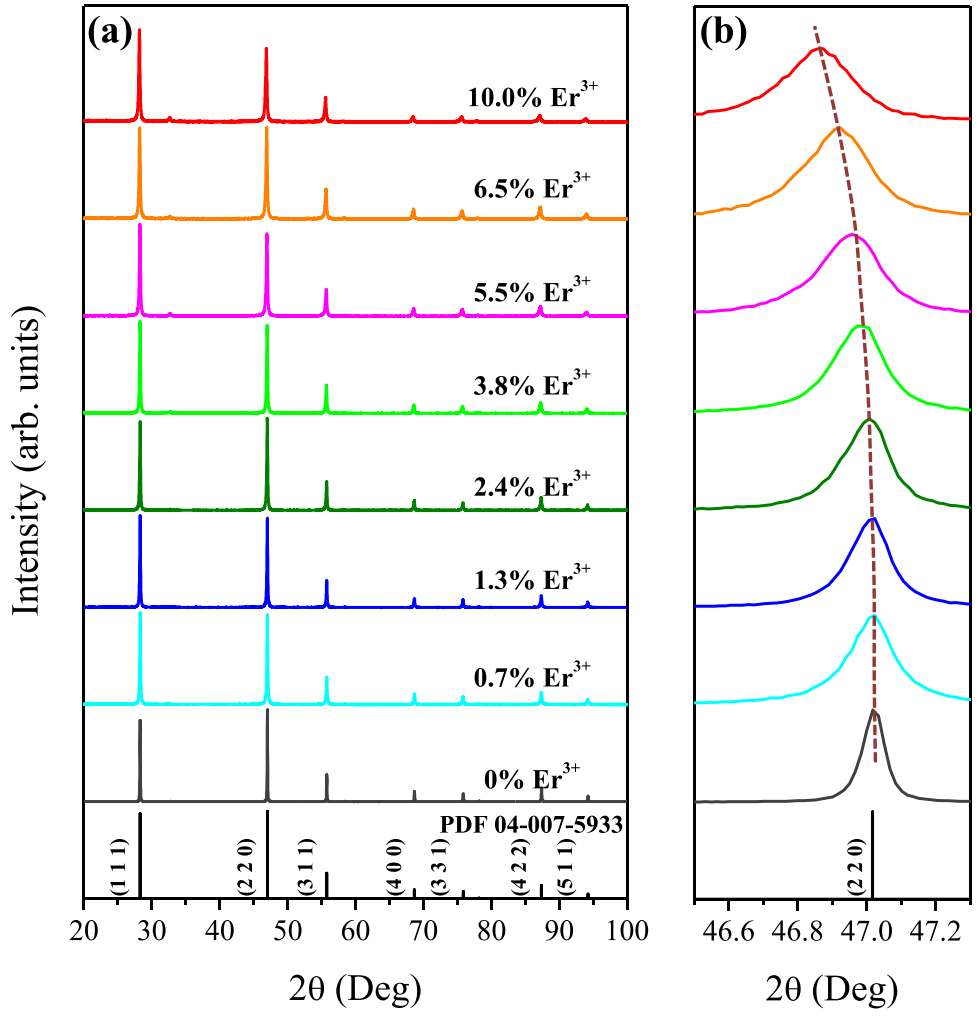

Fig. 1. (a) X-Ray Powder Diffraction (XRD) patterns of the CaF_2:Er^{3+} NPs as function of erbium concentration. (b) Angular shift and broadening of the (2 2 0) difraction peak.

diffraction of the crystalline planes (1 1 1), (2 2 0), (3 1 1), (4 0 0), (3 3 1), (4 2 2) and (5 1 1). These results demonstrate that the synthesized NPs are isostructural with calcium fluoride crystals, with no presence of secondary phases at least up to erbium concentrations of 10 mol%.

As it has been previously observed in other CaF_2:Ln^{3+} NPs [22,24,26,27], the dopant incorporation affects the angular position and width of the diffraction peaks, as it is illustrated in Fig. 1(b) for the (2 2 0) crystalline plane. As it can be seen, the increment of Er^{3+} concentration displaces this diffraction peak to lower angles and simultaneously provokes a progressive broadening. This kind of effects are related to the gradual incorporation of fluorine ions in interstitial positions in order to compensate the extra positive charge that produces the partial cationic substitution of Ca^{2+} ions by Ln^{3+} ions in the lattice.

FullProf Suite open access software from the Institut Laue-Langevin in Grenoble (France) has been used to perform a Rietveld refinement of the measured XRD patterns. Fig. 2 shows the fitted patterns corresponding to NPs with the lower dopant level (0.7 mol %), an intermediate case (3.8 mol%) and the most concentrated NPs (10 mol%).

The Rietveld refinement confirms that the diffraction peaks can be indexed in the fluoride-type structure allowing to access to other relevant information such as lattice parameters, crystallite size and lattice strain. The shift of the diffraction peaks toward smaller angles is associated to a progressive dilatation of the unit cell volume. In Fig. 3(a) the cubic lattice parameter ($a = b = c$) is depicted as function of Er^{3+} concentration. As it can be observed, the lattice parameter increases monotonously with Er^{3+} content, which generates a change in the unit cell volume from 162.92 $(Å)^3$ to 163.70 $(Å)^3$ when erbium concentration increases from 0 mol% to 10 mol%.

The crystallite size (D) and lattice strain (ε) can be estimated from the width of the diffraction peaks (β_{hkl}) by using the Williamson-Hall (W-H) expression [28,29]:

$$\beta_{hkl}\cos\theta = \frac{K\lambda}{D} + 4\varepsilon\sin\theta \quad (1)$$

where K represents a shape factor (equal to 0.94 for cubic crystallites), λ is the X-rays wavelength (0.15406 nm for Cu K_α radiation) and θ corresponds to the angular position of the identified diffraction peaks. Under the W-H formalism the magnitudes ($\beta_{hkl}\cos\theta$) and ($\sin\theta$) are linearly dependent, therefore, a least squares fitting can be used to determine effective values of the crystallite size and lattice strain from selected (hkl) diffraction peaks. The fitting parameters, slope (m) and intersection with the vertical axis (n), are related with the average strain ($m = 4\varepsilon$) and the crystallite size ($D = K\lambda/n$).

In this work, the β_{hkl} values obtained from the Rietveld refinement together with the most intense diffraction peaks, (1 1 1), (2 2 0), (3 1 1), (4 0 0), (3 3 1) and (4 2 2), have been used to determine the crystallite size (D) and lattice strain (ε). The linear fits as function of Er^{3+} concentration are presented in the supplementary material (Fig. S1) where the slope values and y-intersections have been also indicated. The small slope values obtained indicate that the lattice

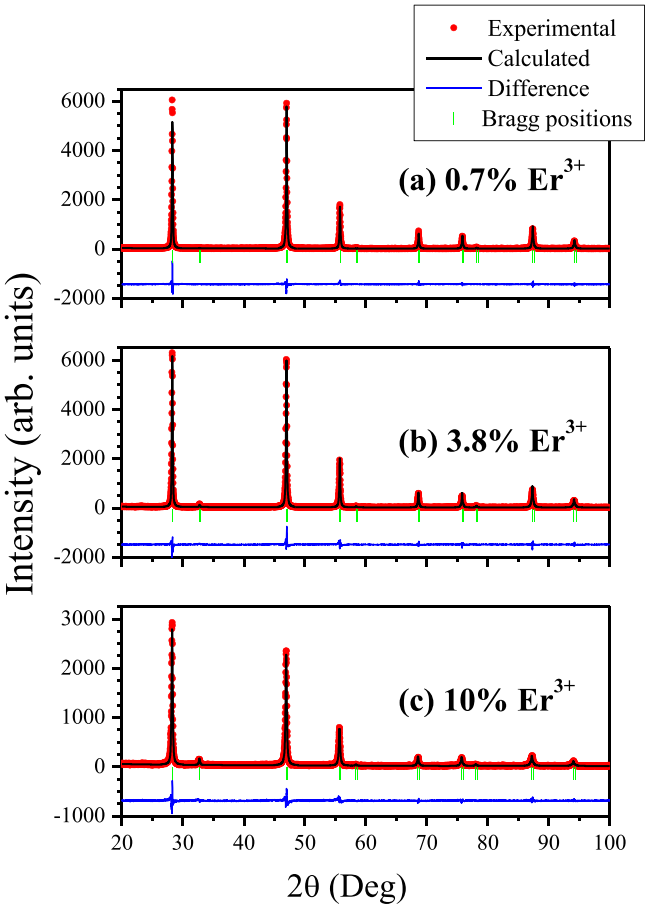

Fig. 2. Rietveld refinement of XRD patterns corresponding to NPs with: (a) the lower doping level (0.7 mol%), (b) an intermediate case (3.8 mol%) and (c) the most concentrated NPs (10 mol%).

strain remains very low, $|\varepsilon| < 0.08\%$, in the concentration range explored in this work, $[Er^{3+}] \leq 10$ mol%.

The dependence of the crystallite size with Er^{3+} content is shown in Fig. 3(b). As it can be observed, the doped NPs exhibit a smaller crystallite size than the undoped ones. In fact, Er^{3+} incorporation provokes an abrupt decrease of the crystallite size which changes from 103 nm (pure CaF_2 NPs) to around 45 nm ($[Er^{3+}]$ = 0.7 mol%). Subsequently, the gradual Er^{3+} incorporation gives rise to a slight reduction of crystallite size as it is summarized in Table 1. The decrease in the crystallite size indicates an increasing trend in the lattice disorder and, therefore, a reduction in the crystallinity. These effects are related to the need to incorporate fluorine ions in interstitial positions to compensate the excess of positive charge generated when Ca^{2+} ions are replaced by Ln^{3+} ions in the CaF_2 lattice, see for instance [18,22].

3.2. Morphology and size distribution

SEM and TEM micrographs were used to characterize the morphology and size distribution of the NPs. The left part of Fig. 4 shows, as an example, a TEM micrograph corresponding to NPs of sample #4; while in the right part the size distributions calculated from micrographs belonging to samples #3, #4 and #7 are presented. As it can be appreciated, NPs exhibit a predominant cubic shape with an overall size distribution that follows a log-normal dependence (red solid lines). The mean particle size obtained from the log-normal distribution of each sample has been included Table 1. From these data it can be said that, independently on the Er^{3+} content, doped

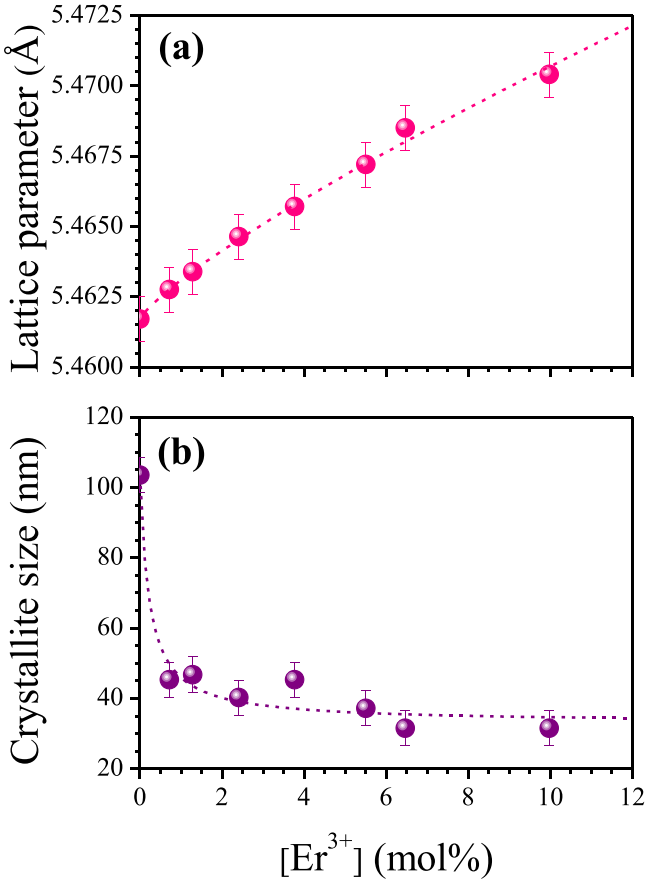

Fig. 3. Cubic lattice parameter and crystallite size as function of Er^{3+} concentration, (a) and (b) respectively. Dashed lines were included to guide the eye.

NPs exhibit an average particle size around 31 nm with a standard deviation of σ = 6nm.

3.3. Photoluminescent characterization: luminescence concentration quenching and radiation trapping

The spectroscopic properties of the Er^{3+}-doped CaF_2 NPs have been investigated under continuous wave excitation (CW) by using an Ar laser (λ = 488nm). As it is depicted in Fig. 5(a), this excitation scheme matches the $^4I_{15/2} \rightarrow {}^4F_{7/2}$ absorption band giving rise, therefore, to the population of this excited state. The relaxation from the $^4F_{7/2}$ level is mainly non-radiative to the thermally coupled multiplets ($^2H_{11/2}$:$^4S_{3/2}$) from where several radiative and non-radiative transitions populate the lower energy levels. Fig. 5(b) shows several cross relaxation mechanisms energetically resonant that affect the population of the different levels. The role of these processes as quenching channels will be discussed latter.

Fig. 6 shows the emission spectra for different Er^{3+} concentrations in the VIS and IR spectral ranges. In the VIS region, Fig. 6(a), the spectra are dominanted by the green emission band associated to the radiative transition $^2H_{11/2}$:$^4S_{3/2} \rightarrow {}^4I_{15/2}$ ($\lambda_{emi} \sim$ 540nm). A closer inspection of this band indicates that the dominant emission arises from the low energy level of the thermally coupled multiplets ($^4S_{3/2}$) while the emission from the upper one ($^2H_{11/2}$) is much weaker, appearing as a shoulder in the lower wavelength spectral region ($\lambda_{emi} \sim$ 520nm). The intensity ratio between these two transitions, $^2H_{11/2} \rightarrow {}^4I_{15/2}$ and $^4S_{3/2} \rightarrow {}^4I_{15/2}$, is related with the local temperature of the sample and it has been widely used as an optical thermometer [30–35]. In particular, the low intensity observed for the $^2H_{11/2} \rightarrow {}^4I_{15/2}$ transition in the Er^{3+}-doped CaF_2 NPs indicates that the $^4I_{15/2} \rightarrow$

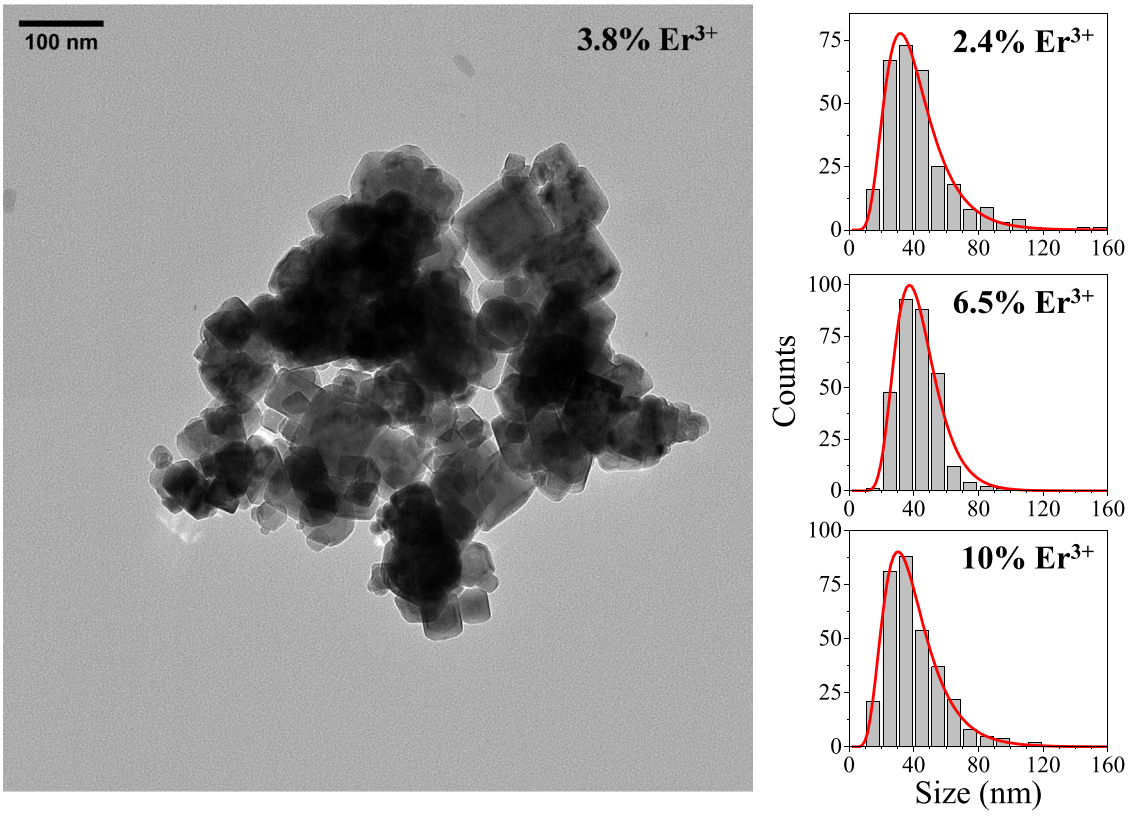

Fig. 4. TEM micrograph corresponding to sample #4 (left), and size distributions calculated for samples #3, #6 and #7 (right); solid red lines represent the fitting to the log-normal distribution.

$^4F_{7/2}$ excitation scheme generates a very low thermal loading to the sample.

Additionally, another transition from $^2H_{11/2}$:$^4S_{3/2}$ multiplets corresponding to the radiative decay to the first excited state ($^4I_{13/2}$) was also detected in the NIR spectral range ($\lambda_{emi} \sim 850$ nm), see Fig. 6(b). The radiative de-excitation from the $^4I_{13/2}$ level to the ground state gives rise to the 1.5 µm emission band characteristic of Er ions, $^4I_{13/2} \rightarrow {}^4I_{15/2}$, which is the dominant band in the IR spectral region.

Two additional emission bands appear in the spectra centred at around $\lambda_{emi} \sim 670$ nm and $\lambda_{emi} \sim 1.0$ µm. These bands can be associated to the $^4F_{9/2} \rightarrow {}^4I_{15/2}$ and $^4I_{11/2} \rightarrow {}^4I_{15/2}$ transitions, respectively. As it will be proved later, in spite of the low energy phonon of CaF_2 ($\hbar\Omega = 328 cm^{-1}$ [10]), both emitting levels, $^4F_{9/2}$ and $^4I_{11/2}$, receive population through the non-radiative connections from the upper levels, $^4S_{3/2}$ and $^4I_{9/2}$ respectively.

As it is apparent from Fig. 6, the different emission bands present the same dependency on the Er^{3+} content: initially the intensity increases as the concentration increases, it reaches the maximum value when $[Er^{3+}] = 3.8$ mol% ($N_{Er} = 9.3 \times 10^{20}$ cm^{-3}) and then it enters in a decreasing stage with the concentration. The emission

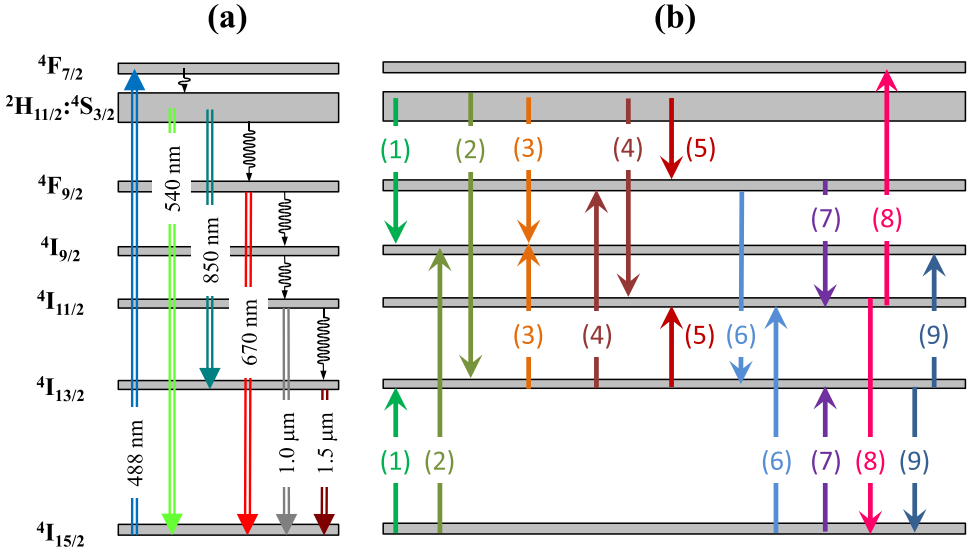

Fig. 5. (a) Partial energy level diagram of Er^{3+} ions showing the excitation scheme together with the dominant transitions observed in the CW photoluminescent characterization. (b) Cross relaxation mechanisms energetically resonant that affect the population of the different levels.

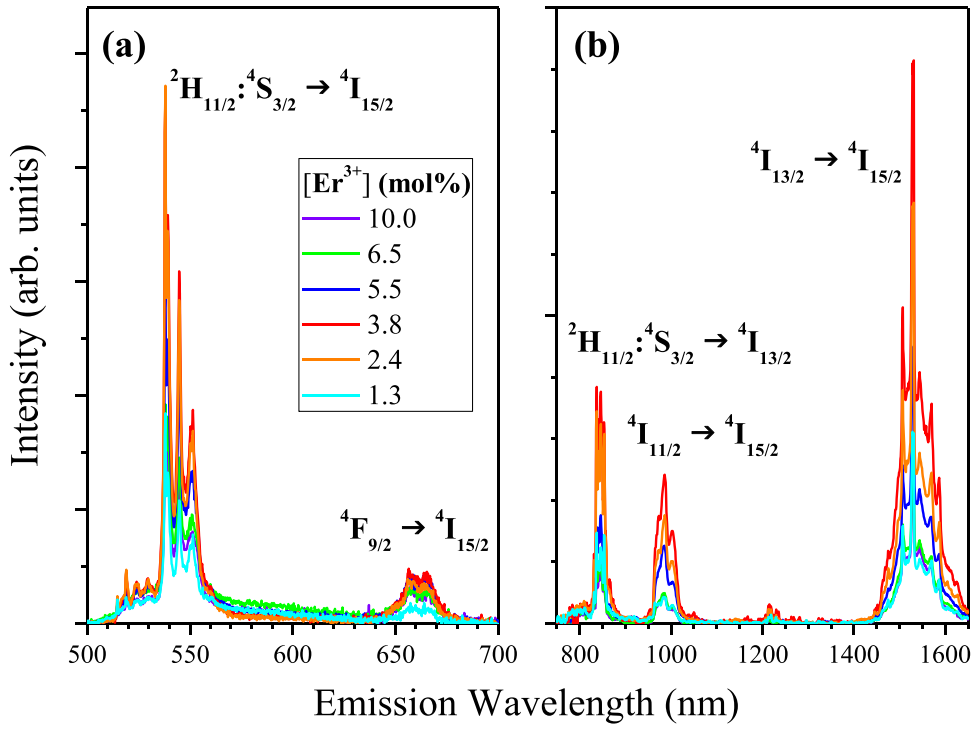

Fig. 6. Dominant emission bands detected in the VIS and IR spectral ranges under CW excitation at 488 nm, (a) and (b) respectively.

intensity of the different transitions, calculated as the area of the emission band, is presented in Fig. 7 in a double logarithmic scale.

In general, the intensity (I) of an emission band is porportional to the product of the active ion concentration (N) and the luminescence quantum efficiency (η) of the emitting manifold, that is:

$$I = K_n \eta N \tag{2}$$

where K_n is a normalization constant that depends on the experimental conditions such as excitation and collection geometry.

A careful inspection of the figure reveals that in diluted samples the luminescence intensity increases linearly with the Er^{3+} content, while in the opposite limit, when Er^{3+} concentration exceeds 3.8 mol %, the emission intensity decreases as the dopant level increases. This situation is a clear indicative of the activation of luminescence quenching mechanisms, also known as self-quenching processes (apparition of ion-ion interactions, diffusion and cross relaxation mechanisms, that become active when dopant level surpasses a certain critical value) [3,36]. Thus, in highly doped samples, there is a competition between the spontaneous relaxation channels (radiative and non-radiative) and the luminescence quenching processes. Although Eq. (2) can not be applied to describe such kind of situations, it can be rewritten to include the presence of quenching processes.

The luminescence quantum efficiency (η_d) is calculated in diluted samples as:

$$\eta_d = A_{rad}/A_0 \tag{3}$$

where A_{rad} is the radiative transition probability and $A_0 = A_{rad} + W_{NR}$ represents the total transition probability; that is the sum of the radiative and non-radiative (W_{NR}) probabilities.

When concentration quenching processes are activated, their probability (W_Q) must be also take into account. Therefore, the luminescence quantum efficiency (η) in this case must be evaluated as:

$$\eta = A_{rad}/(A_0 + W_Q) \tag{4}$$

Instead of the above absolute values, it is more convenient to use a relative efficiency (η_{rel}), taking as reference the value in diluted samples, defined by [37]:

$$\eta_{rel} = \frac{\eta}{\eta_d} = \frac{A_0}{A_0 + W_Q} \tag{5}$$

Considering the relative efficiency, Eq. (2) can be rewritten as:

$$I = K'_n \eta_{rel} N \tag{6}$$

where the normalization constant has been now redefined as $K'_n = K_n \eta_d$. In relation to the quenching process, its probability is found to depend in many cases of some power of the dopant level [3,38] ($W_Q = VN^{s/3}$), thus:

$$I = K'_n \frac{A_0 N}{A_0 + VN^{s/3}} = K'_n \frac{N}{1 + (N/N_C)^{s/3}} \tag{7}$$

where s indicates the multipole order of interaction involved in the transfer process that can be 6, 8, 10, ... for dipole-dipole, dipole-quadrupole, quadrupole-quadrupole, ... interactions.

Additionally, in Eq. (7), it has been defined for convenience the N_C parameter, ($N_C^{s/3} = A_0/V$), that represents a critical concentration value at which the relative quantum efficiency is reduced to 50%, or, in other words, a concentration at which the concentration quenching rate equals the intrinsic (low concentration) relaxation rate ($A_0 = W_Q$).

The intensity of the different Er^{3+} emission bands has been analized in terms of Eq. (7). A least squares fitting was performed (dashed lines in Fig. 7) to determine the different parameters (K'_n, N_C and s) that appear in this expression. The best fit was obtained with the parameters presented in Table 2.

As it can be seen, while all the emission intensities can be fitted by using the same critical concentration, $N_C = 1.28 \times 10^{21}$ cm^{-3} (5.2 mol%), the normalization constant and the multipole order of the interaction are dependent on each transition. The values of the first one (K'_n) account for the relative intensity of each emission while the second one (s) indicates the multipolar order of the quenching process [8,9,37,38]. As it is indicated in Table 2, the

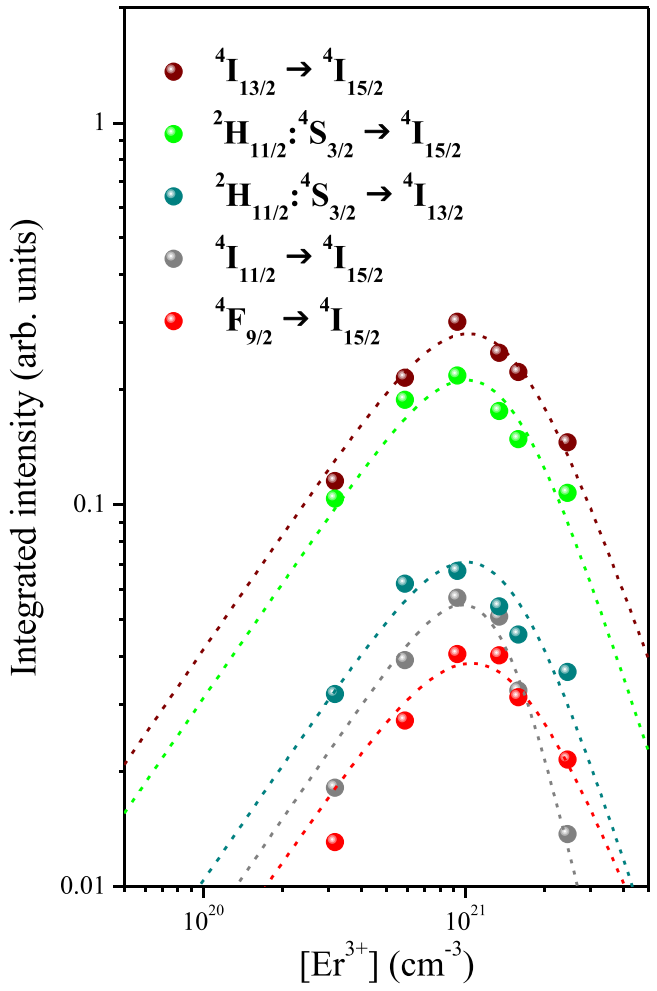

Fig. 7. Integrated emission intensity as function of the Er^{3+} concentration. Dashed lines represent the least squares fitting to Eq. (7).

Table 2
Parameters obtained by fitting the emission intensities to Eq. (7).

Manifold	K'_n (10^{-22} cm^3)	N_C (10^{21} cm^{-3})	s
$^4I_{13/2}$	4.17	1.28	8.7
$^4I_{11/2}$	0.75	1.28	12.0
$^2H_{11/2}$:$^4S_{3/2}$	3.11	1.28	9.3
$^4F_{9/2}$	0.58	1.28	8.1

intensity of none of the transitions can be adjusted considering quenching processes operating under dipole-dipole interaction ($s = 6$). In fact, under CW excitation, these mechanisms seem to operate under different multipolar interactions: the luminescent quenching processes affecting the $^4I_{13/2}$ and $^4F_{9/2}$ levels exhibit an exponent close to the dipole-quadrupole interaction ($s = 8$), the exponent of the mechanisms that reduce the intensity of the luminescence from the green emitting levels, $^2H_{11/2}$:$^4S_{3/2}$, is slightly lower than the corresponding to the quadrupole-quadrupole interaction ($s = 10$) and, finally, the quenching of the $^4I_{11/2}$ level seems to operate under quadrupole-hexapole interaction ($s = 12$).

The differences in the multipolar order of the quenching processes that affect each level could be related to the different cross relaxation mechanisms that are operative under a certain excitation scheme. In Fig. 5(b) several cross relaxation processes, all of them active under CW excitation, are proposed. These mechanisms should present a high efficiency due to their energetically resonant character. As it can be seen, mechanisms (1) to (5) lead to a severe depopulation of the green emitting levels while they populate the lower energy levels. Similarly, the processes labelled as (6) and (7) in figure reduce the population of the $^4F_{9/2}$ level, producing a net increment in the steady state population of $^4I_{11/2}$ and $^4I_{13/2}$ erbium levels. Finally, the cross relaxation processes (8) and (9), that in fact are up-conversion mechanisms, give rise to a depletion of the population in the intermediate levels ($^4I_{11/2}$ and $^4I_{13/2}$) which is sent to the ground state ($^4I_{15/2}$) and to the upper levels ($^4F_{7/2}$ and $^4I_{9/2}$). Therefore, looking at a certain level, it can simultaneously play the role of donor and acceptor level. Consequently, the multipolar order (s-exponent) obtained from the fitting provides an effective value that encompasses all the cross relaxation processes that affect the level under consideration.

On the other hand, as it has been indicated in the introduction section, the luminescence quenching processes affects both the emission intensities under steady state conditions (CW excitation) as well as to the population dynamics under pulsed excitation. Therefore, in order to further study the concentration quenching, the luminescent temporal decays of the different emitting levels have been investigated.

The temporal decay of the green emission band ($^2H_{11/2}$:$^4S_{3/2} \rightarrow {}^4I_{15/2}$) was measured under resonant excitation by using the second harmonics of a Nd:YAG laser (λ_{exc} = 532 nm, pulse width 10 ns). The corresponding temporal decays are presented in Fig. 8(a) for selected Er^{3+} concentrations, [Er^{3+}] = 2.4, 6.5 and 10 mol%.

Experimentally, it was observed that the excitation to the $^2H_{11/2}$:$^4S_{3/2}$ multiplets gives rise to a very weak population of the lower liying levels. Then, the luminescent temporal decay from the $^4F_{9/2}$ level was explored under excitation at λ_{exc} = 650 nm ($^4I_{15/2} \rightarrow {}^4F_{9/2}$ absorption band) by using a laser diode electronically switched to provide pulsed excitation. Under this excitation scheme not only the red emission can be detected but also those centred at 1.0 µm and 1.5 µm, arising from the deexcitation of $^4I_{11/2}$ and $^4I_{13/2}$ manifolds to the ground state. Let us remark that this excitation procedure, using an externally driven switch of the excitation, provides the possibility of selecting an adjustable dark window which guarantees a full decay of the luminescent signals, needed for the addequate measurement of the decay times of these long living emitting levels. The temporal decays corresponding to the transitions from the $^4F_{9/2}$, $^4I_{11/2}$ and $^4I_{13/2}$ manifolds to the ground state are presented in Fig. 8(b), Fig. 8(c) and Fig. 8(d) respectively. For clarity reasons, Fig. 8(b) only includes the decays for two different erbium concentrations, [Er^{3+}] = 2.4 and 10 mol%.

As it can be observed all the decays exhibit a non-exponential behaviour with average decay times covering a broad range. The fastest decays correspond to the red emission ($^4F_{9/2} \rightarrow {}^4I_{15/2}$) having a characteristic decay time $\tau_{1/e} \sim 0.1$ms and the green one ($^2H_{11/2}$:$^4S_{3/2} \rightarrow {}^4I_{15/2}$) with $\tau_{1/e} \sim 0.3 - 0.1$ms. The infrared emissions exhibit substantially longer decays in the range $\tau_{1/e} \sim 8 - 3$ms and $\tau_{1/e} \sim 15 - 6$ms for the $^4I_{11/2}$ and $^4I_{13/2}$ manifolds, respectively. In fact, it is clear in Fig. 8 that the luminescent decays are concentration dependent, being faster in NPs with higher dopant levels and all of them can be described using a bi-exponential function (solid lines in figure):

$$I(t) = I_1\exp(-t/\tau_1)+I_2\exp(-t/\tau_2) \quad (8)$$

where I_1 and I_2 represent the intensity of the corresponding exponential component having decay times τ_1 and τ_2, parameters which are concentration dependent. The corresponding fitting parametes are summarized in Table 3 together with an effective decay time (τ_{eff}) defined as [39]:

$$\tau_{eff} = \frac{1}{I(0)}\int_0^\infty I(t)dt = \frac{I_1\tau_1 + I_2\tau_2}{I_1 + I_2} \quad (9)$$

The data shown in Table 3 reveal that the time constants τ_1, τ_2 and τ_{eff} of the different emitting manifolds present a general decreasing

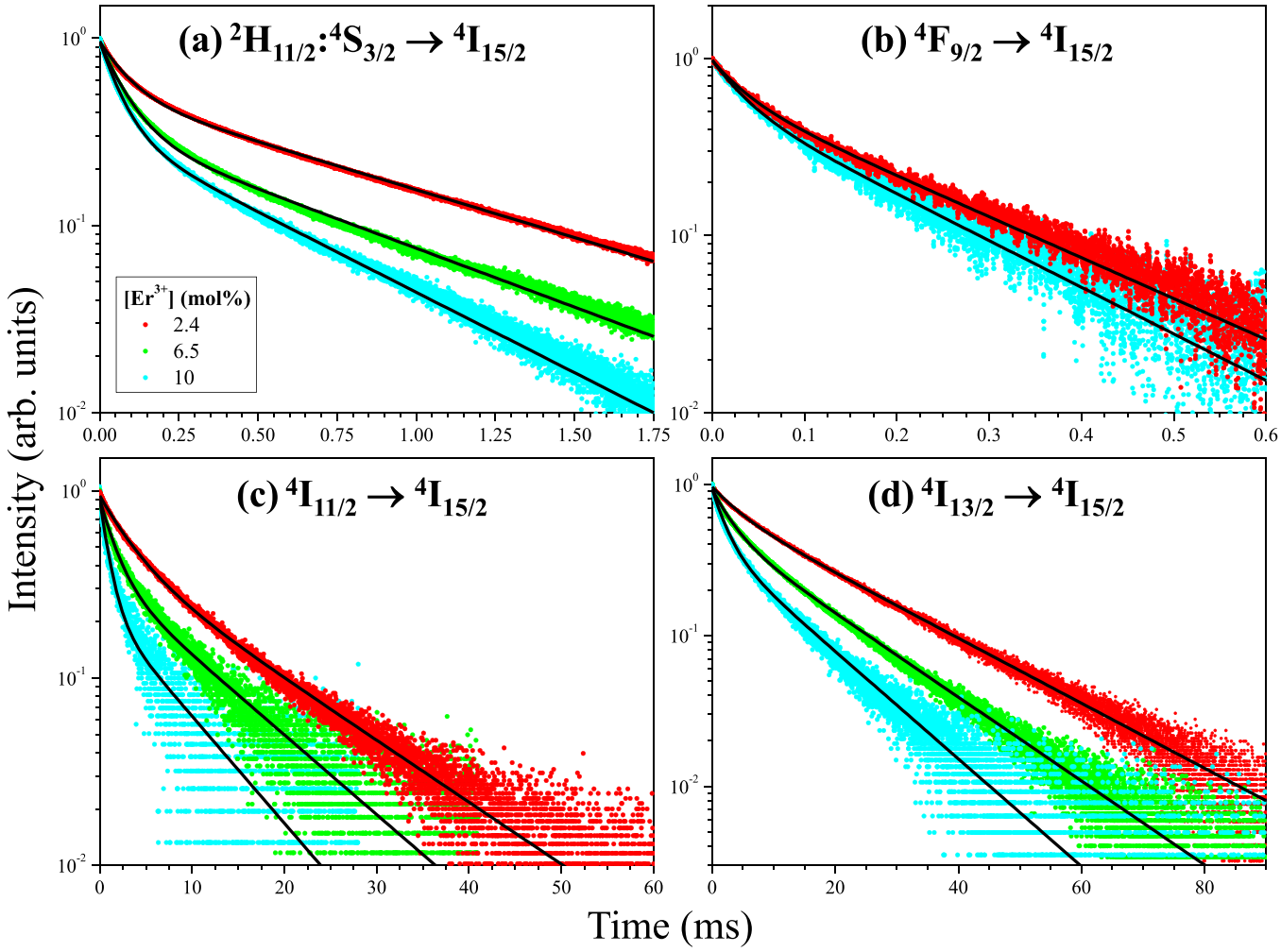

Fig. 8. Luminescent temporal decays of (a) $^2H_{11/2}$:$^4S_{3/2}$ → $^4I_{15/2}$, (b) $^4F_{9/2}$ → $^4I_{15/2}$, (c) $^4I_{11/2}$ → $^4I_{15/2}$ and (d) $^4I_{14/2}$ → $^4I_{15/2}$ Er^{3+} transitions.

trend when Er^{3+} concentration is higher than 2.4mol%. Nevertheless, in diluted NPs ($N_{Er} \leq$ 2.4mol%) the time constants slightly increase when the dopant level increases. Although this behaviour is observed for all the emitting levels, it is more evident in the case of the first excited state, $^4I_{13/2}$, as it exhibits the highest decay time. This kind of tendency with concentration has been previously reported in other rare-earth doped materials and it has been associated to the simultaneous presence of radiation trapping and concentration quenching [8]. If only luminescence quenching processes affect the temporal decays, then the effective decay time can be obtained from the total transition probability by:

$$\tau_{eff} = \frac{1}{A_T} = \frac{1}{A_0 + W_Q} = \frac{1}{A_0} \times \frac{1}{1 + (N/N_C)^{s/3}} \quad (10)$$

Eq. (10) indicates that the effective decay time should be constant in diluted samples, where concentration quenching can be neglected, while for higher dopant levels it should exhibit a decreasing tendency as concentration increases. As it has been previously commented, the data shown in Table 3 reveals that the effective decay time increases at low concentration, reaches a maximum value and then decreases monotonously as it is expected according to Eq. (11). This initial growth stage at low dopant levels is caused by radiation trapping [8] (emitted radiation is reabsorbed and re-emitted again, resulting in an increase in the decay time).

When the decays are also affected by radiation trapping, Eq. (10) should be modified in order to include such effects. In these cases, the effective decay time depends on the dopant level as [8]:

$$\tau_{eff} = \frac{1}{A_0} \times \frac{1 + \sigma l N}{1 + (N/N_C)^{s/3}} \quad (11)$$

where σ represents the absorption cross section and l is an average absorption length. In Eqs. (10) and (11), N_C and s have the same meaning than in Eq. (7).

Fig. 9 shows the effective decay time of the emitting manifolds as function of Er^{3+} concentration. As it can be seen all the emitting manifolds exhibit a common trend, the decay time increases slightly up to erbium concentration around $N_{Er} \approx 6 \times 10^{20}$ ions/cm^3 ([Er^{3+}] = 2.4 mol%) and then monotonously decrease as dopant level increases. Dashed lines in the figure correspond to the best least squares fitting to Eq. (11) considering that the critical concentration has the value obtained under CW excitation, $N_C = 1.28 \times 10^{21}$ cm^{-3}. The fitting parameters (A_0, σl and s) are summarized in Table 4 together with the lifetime value of each emitting level in absence of radiation trapping and quenching processes ($\tau_0 = A_0^{-1}$).

Comparing Tables 2 and 4, it is clear that the multipole order of interaction is different depending on whether the excitation is carried out in CW or pulsed mode. In fact, under pulsed excitation, the fitting indicates that the quenching processes affecting $^4I_{11/2}$, $^2H_{11/2}$:$^4S_{3/2}$ and $^4F_{9/2}$ levels seem to operate under dipole-dipole type interactions ($s \sim 6$) while the mechanisms affecting the $^4I_{13/2}$ manifold are basically of the dipole-quadrupole type ($s \sim 8$). These differences in the multipole order, compared with those obtained under CW excitation, could be caused by the activation and/or disconnection of

Table 3
Parameters obtained by fitting the luminescent temporal decays to bi-exponential functions and effective decay times calculated according to Eq. (9).

Manifold	Er^{3+} (mol%)	I_1	τ_1 (ms)	I_2	τ_2 (ms)	τ_{eff} (ms)
$^2H_{11/2}$:$^4S_{3/2}$	0.7	77.2	88.0×10^{-3}	22.8	899×10^{-3}	273×10^{-3}
	1.3	69.8	84.9×10^{-3}	30.2	892×10^{-3}	329×10^{-3}
	2.4	71.9	87.4×10^{-3}	28.1	852×10^{-3}	302×10^{-3}
	3.8	76.8	83.2×10^{-3}	23.2	814×10^{-3}	253×10^{-3}
	5.5	81.2	81.8×10^{-3}	18.8	733×10^{-3}	204×10^{-3}
	6.5	85.5	80.2×10^{-3}	14.5	691×10^{-3}	169×10^{-3}
	10	89.4	62.3×10^{-3}	10.6	506×10^{-3}	109×10^{-3}
$^4F_{9/2}$	0.7	64.8	33.5×10^{-3}	35.2	192×10^{-3}	89×10^{-3}
	1.3	58.0	33.5×10^{-3}	42.0	190×10^{-3}	99×10^{-3}
	2.4	47.2	33.4×10^{-3}	52.8	188×10^{-3}	115×10^{-3}
	3.8	56.7	33.3×10^{-3}	43.3	187×10^{-3}	100×10^{-3}
	5.5	50.7	33.1×10^{-3}	49.3	182×10^{-3}	107×10^{-3}
	6.5	58.5	33.0×10^{-3}	41.5	180×10^{-3}	94×10^{-3}
	10	53.7	32.3×10^{-3}	46.3	165×10^{-3}	94×10^{-3}
$^4I_{11/2}$	0.7	53.3	2.9	46.7	13.8	8.0
	1.3	49.6	3.1	50.4	13.8	8.5
	2.4	51.5	3.2	48.5	13.1	8.0
	3.8	58.5	2.4	41.5	12.0	6.4
	5.5	61.9	2.1	38.1	11.4	5.6
	6.5	60.9	1.7	39.1	10.2	5.0
	10	74.0	1.0	26.0	7.6	2.7
$^4I_{13/2}$	0.7	54.3	4.10	45.7	21.0	11.8
	1.3	35.3	4.15	64.7	20.5	14.7
	2.4	27.7	4.31	72.3	20.2	15.8
	3.8	33.5	3.87	66.5	20.0	14.6
	5.5	34.6	3.52	65.4	17.2	12.5
	6.5	45.7	3.17	54.3	15.6	9.9
	10	56.7	2.03	43.3	12.2	6.4

different cross relaxation mechanisms depending on whether the active ions are in a steady state (CW excitation) or in a transient state (pulsed excitation), see Fig. 5(b).

3.4. Judd-Ofelt analysis

In this last section the erbium transition probabilities are estimated according to the theory developed by Judd [40] and Ofelt [41].

The standard Judd-Ofelt (JO) procedure requires to know the absorption cross sections of at least three absorption bands in order to quantify the three JO intensity parameters, $\Omega_t (t = 2, 4, 6)$. In the case of powder samples, as it is the case of the CaF_2:Er^{3+} NPs, it is difficult to accurately determine the sample thickness and it is not possible to calibrate the absorption spectrum in terms of absorption cross sections; therefore, the standard JO procedure is not applicable. However, as it has been previously demonstrated [42,43], in these cases it is possible to use a modified JO procedure to obtain proportional intensity parameters (ω_t) that are related to the JO intensity parameters by:

$$\omega_t = C_{JO} \times \Omega_t \ (t = 2, 4, 6) \tag{12}$$

where C_{JO} is a proportionality constant that relates the absolute and relative line strengths values. The value of this constant can be estimated from the probability of a purely radiative transition of the active ion, making it possible to determine the JO intensity parameters $\Omega_t (t = 2, 4, 6)$ by using Eq. (12). The details of the calculation method are described in [42].

The JO analysis has been performed using the absorption spectrum shown in Fig. 10, corresponding to CaF_2 NPs doped with [Er^{3+}] = 2.4 mol%. The inset shows the comparison between the relative values obtained for the experimental ($S^{rel}_{ed,exp}$) and theoretical ($S^{rel}_{ed,th}$) electric dipole line strengths, calculated by using the reduced matrix elements reported for Er^{3+} ions [44] and the Sellmeier dispersion formula of CaF_2 [45].

The relative values obtained for the experimental ($S^{rel}_{ed,exp}$) and theoretical ($S^{rel}_{ed,exp}$) electric dipole line strengths and the

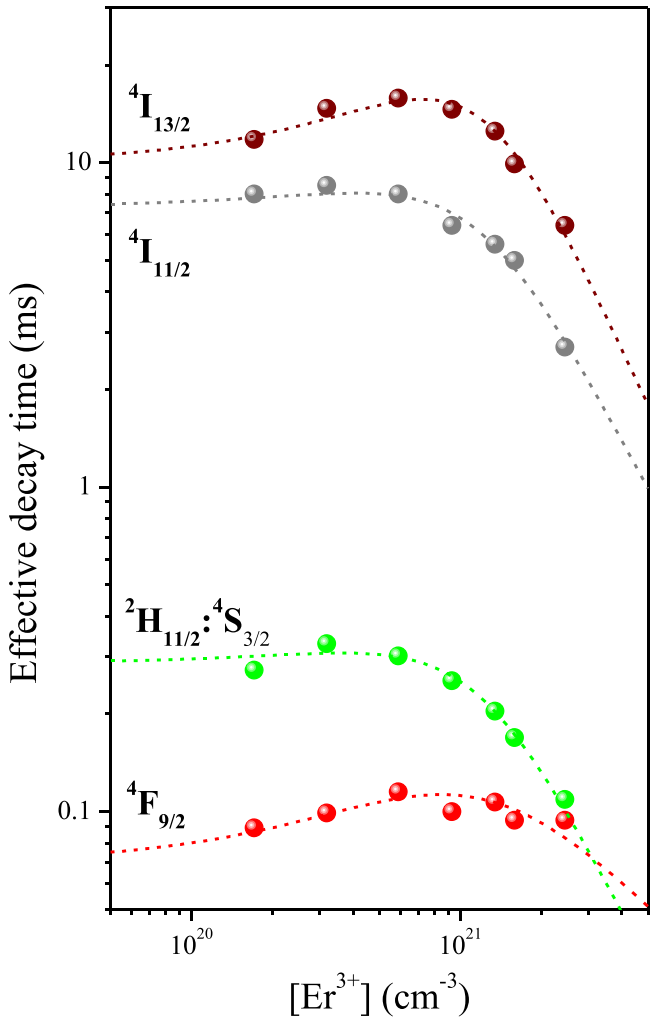

Fig. 9. Effective decay times of the main emitting manifolds. Dashed lines represent the fitting to Eq. (11).

Table 4
Parameters obtained by fitting the effective decay times to Eq. (11).

Manifold	A_0 (s^{-1})	τ_0 (ms)	σl (10^{-21} cm^3)	s
$^4I_{13/2}$	100	10	1.25	8.1
$^4I_{11/2}$	137	7.3	0.45	6.9
$^2H_{11/2}$: $^4S_{3/2}$	3496	0.286	0.38	6.9
$^4F_{9/2}$	14400	0.069	1.65	5.4

proportional Judd-Ofelt intensity parameters $\omega_t (t = 2, 4, 6)$ are summarized in Table 5 together with the root-mean-square deviation of the fit.

The low energy phonon of CaF_2 ($\hbar\Omega = 328cm^{-1}$ [10]) ensures that the energy difference between the first excited state, $^4I_{13/2}$ level, and the ground state ($\Delta E \sim 6540cm^{-1}$) is high enough to neglect the multiphonon relaxations. On the other hand, the treatment carried out in previous section allows establishing that the total transition probability of $^4I_{13/2}$ level is $A_{rad} = A_0 = 100s^{-1}$ in absence of self-quenching and radiation trapping. This value has been used to determine that in CaF_2:Er^{3+} NPs the JO intensity parameters are $\Omega_{2,4,6}$=1.97, 0.91 and 1.34 in units of 10^{-20} cm^2. In the supplementary material, these values are compared with the intensity parameters previously reported in Er^{3+}-doped CaF_2 crystals [39,46] and in transparent ceramics based on this material [47]. As it is shown in Fig. S2., the Ω_t-parameters seem to be dependent on the nature of the sample. Additionally, and in relation to the radiative lifetime

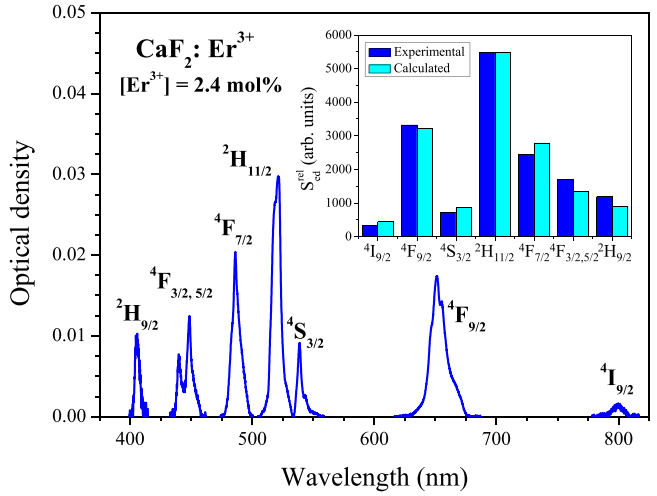

Fig. 10. Absorption spectrum of Er^{3+} ions in the CaF_2 NPs. The inset shows the relative values of the experimental and calculated dipole line strengths.

Table 5
Relative values of the experimental and theoretical electric dipole line strengths and proportional Judd-Ofelt intensity parameters (ω_t) of Er^{3+}-doped CaF_2 nanoparticles.

Transition	Barycentre (cm^{-1})	$S^{rel}_{ed,exp}$ (arb. units)	$S^{rel}_{ed,th}$ (arb. units)	ΔS^{rel}_{ed} (arb. units)
$^4I_{15/2} \rightarrow {}^4I_{9/2}$	12517	323.38	441.07	-117.69
$^4I_{15/2} \rightarrow {}^4F_{9/2}$	15305	3317.93	3205.98	111.96
$^4I_{15/2} \rightarrow {}^4S_{3/2}$	18501	722.91	852.29	-129.38
$^4I_{15/2} \rightarrow {}^2H_{11/2}$	19231	5465.22	5465.22	0.00
$^4I_{15/2} \rightarrow {}^4F_{7/2}$	20530	2440.78	2784.20	-343.42
$^4I_{15/2} \rightarrow {}^4F_{3/2,5/2}$	22396	1702.27	1331.48	370.79
$^4I_{15/2} \rightarrow {}^2H_{9/2}$	24624	1185.71	885.72	299.99
$\omega_2 = 5.63 \times 10^3$ arb. units				
$\omega_4 = 2.61 \times 10^3$ arb. units				
$\omega_6 = 3.83 \times 10^3$ arb. units				
rms $(\Delta S^{rel}_{ed}) = 311.66$		rms (ΔS^{rel}_{ed}) / rms $(\Delta S^{rel}_{ed,exp}) = 8.7\%$		

value obtained for the $^4I_{13/2}$ metastable level, $\tau_{rad} = A_0^{-1} = 10$ms, it should be noted that it is higher than the value reported for crystalline samples, $\tau_{rad} = 7.6 - 7.7$ms [39,46], but lower that those found in transparent ceramics, $\tau_{rad} = 13.2$ms [47].

The electric dipole contribution (A_{ed}) to the total radiative transition rate from an excited J manifold to the lower J' levels can be evaluated by using the Ω_t intensity parameters and the reduced matrix elements, $|\langle \phi J | |U^{(t)}| | \phi' J' \rangle|^2$, by:

$$A_{ed}(J \rightarrow J') = \frac{64\pi^4 e^2}{3h(2J+1)\lambda_m^3} \frac{n(n^2+2)^2}{9} \sum_{t=2,4,6} \Omega_t \, |\langle \phi J | |U^{(t)}| | \phi' J' \rangle|^2 \quad (13)$$

where h is the Planck's constant, λ_m is the barycenter wavelength and n the refractive index at λ_m.

The magnetic dipole contributions (A_{md}) were calculated as in reference [38]. The results are summarized in Table 6 where radiative lifetimes and branching ratios have also been included.

As the $^2H_{11/2}$ and $^4S_{3/2}$ levels are thermally coupled at room temperature, they exhibit a common radiative lifetime that can be evaluated as:

$$\frac{1}{\tau_{rad}} = \frac{g_H A^H_{rad} \exp(-\Delta E/kT) + g_S A^S_{rad}}{g_H \exp(-\Delta E/kT) + g_S} \quad (14)$$

where g_H and g_S symbolize the degeneracy of $^2H_{11/2}$ and $^4S_{3/2}$ levels, A^H_{rad} and A^S_{rad} their radiative transition probabilities, $\Delta E = 729 cm^{-1}$ is the energy gap between both levels [44], k represents the Boltzmann's constant and $T = 300$K is the room temperature.

Table 6
Calculated electric dipole (A_{ed}) and magnetic dipole (A_{md}) transition probabilities, radiative lifetimes ($\tau^{-1}_{rad} = \Sigma_{J'} A_T(J \rightarrow J')$) and branching ratios ($\beta = \tau_{rad} A_T(J \rightarrow J')$).

Transition	A_{ed} (s^{-1})	A_{md} (s^{-1})	τ_{rad} (μs)	β (%)
$^4G_{11/2} \rightarrow {}^2H_{9/2}$	0		118	0
$^4G_{11/2} \rightarrow {}^4F_{5/2,3/2}$	2			0
$^4G_{11/2} \rightarrow {}^4F_{7/2}$	9			0
$^4G_{11/2} \rightarrow {}^2H_{11/2}$	11	9		0
$^4G_{11/2} \rightarrow {}^4S_{3/2}$	9			0
$^4G_{11/2} \rightarrow {}^4F_{9/2}$	190	2		2
$^4G_{11/2} \rightarrow {}^4I_{9/2}$	68	1		1
$^4G_{11/2} \rightarrow {}^4I_{11/2}$	41			0
$^4G_{11/2} \rightarrow {}^4I_{13/2}$	976	32		12
$^4G_{11/2} \rightarrow {}^4I_{15/2}$	7139			85
$^2H_{9/2} \rightarrow {}^4F_{5/2,3/2}$	0		529	0
$^2H_{9/2} \rightarrow {}^4F_{7/2}$	3	1		0
$^2H_{9/2} \rightarrow {}^2H_{11/2}$	8	1		0
$^2H_{9/2} \rightarrow {}^4S_{3/2}$	0			0
$^2H_{9/2} \rightarrow {}^4F_{9/2}$	15	32		2
$^2H_{9/2} \rightarrow {}^4I_{9/2}$	12	1		1
$^2H_{9/2} \rightarrow {}^4I_{11/2}$	155	26		10
$^2H_{9/2} \rightarrow {}^4I_{13/2}$	766			40
$^2H_{9/2} \rightarrow {}^4I_{15/2}$	873			47
$^4F_{5/2,3/2} \rightarrow {}^4F_{7/2}$	0		278	0
$^4F_{5/2,3/2} \rightarrow {}^2H_{11/2}$	1			0
$^4F_{5/2,3/2} \rightarrow {}^4S_{3/2}$	1	4		0
$^4F_{5/2,3/2} \rightarrow {}^4F_{9/2}$	76			2
$^4F_{5/2,3/2} \rightarrow {}^4I_{9/2}$	184			5
$^4F_{5/2,3/2} \rightarrow {}^4I_{11/2}$	646			18
$^4F_{5/2,3/2} \rightarrow {}^4I_{13/2}$	812			23
$^4F_{5/2,3/2} \rightarrow {}^4I_{15/2}$	1879			52
$^4F_{7/2} \rightarrow {}^2H_{11/2}$	0		420	0
$^4F_{7/2} \rightarrow {}^4S_{3/2}$	0			0
$^4F_{7/2} \rightarrow {}^4F_{9/2}$	2	9		0
$^4F_{7/2} \rightarrow {}^4I_{9/2}$	80	8		4
$^4F_{7/2} \rightarrow {}^4I_{11/2}$	113			5
$^4F_{7/2} \rightarrow {}^4I_{13/2}$	199			8
$^4F_{7/2} \rightarrow {}^4I_{15/2}$	1968			83
$^2H_{11/2} \rightarrow {}^4S_{3/2}$	0		438	0
$^2H_{11/2} \rightarrow {}^4F_{9/2}$	6			0
$^2H_{11/2} \rightarrow {}^4I_{9/2}$	37			2
$^2H_{11/2} \rightarrow {}^4I_{11/2}$	26	6		1
$^2H_{11/2} \rightarrow {}^4I_{13/2}$	54	47		4
$^2H_{11/2} \rightarrow {}^4I_{15/2}$	2107			93
$^4S_{3/2} \rightarrow {}^4F_{9/2}$	0		775	0
$^4S_{3/2} \rightarrow {}^4I_{9/2}$	37			3
$^4S_{3/2} \rightarrow {}^4I_{11/2}$	26			2
$^4S_{3/2} \rightarrow {}^4I_{13/2}$	361			28
$^4S_{3/2} \rightarrow {}^4I_{15/2}$	866			67
$^4F_{9/2} \rightarrow {}^4I_{9/2}$	0	2	1212	0
$^4F_{9/2} \rightarrow {}^4I_{11/2}$	42	4		6
$^4F_{9/2} \rightarrow {}^4I_{13/2}$	34			4
$^4F_{9/2} \rightarrow {}^4I_{15/2}$	743			90
$^4I_{9/2} \rightarrow {}^4I_{11/2}$	0	1	10420	1
$^4I_{9/2} \rightarrow {}^4I_{13/2}$	39			41
$^4I_{9/2} \rightarrow {}^4I_{15/2}$	56			58
$^4I_{11/2} \rightarrow {}^4I_{13/2}$	14	7	8524	18
$^4I_{11/2} \rightarrow {}^4I_{15/2}$	96			82
$^4I_{13/2} \rightarrow {}^4I_{15/2}$	72	28	10000	100

In this point it is important to remark that the total transition probabilities shown in Table 4 include the radiative and non-radiative contributions ($A_0 = A_{rad} + W_{NR}$). Taking into account that the radiative transition probability can be calculated from the radiative lifetime ($A_{rad} = 1/\tau_{rad}$) shown in Table 6, the non-radiative probability can be estimated for the $^4F_{9/2}$, $^2H_{11/2}$:$^4S_{3/2}$ and $^4I_{11/2}$ manifolds.

On the other hand, the non-radiative transition probabilities are related with the energy difference (ΔE) between the two levels involved in the transition through the gap law:

$$W_{NR} = C \exp(-\alpha \Delta E) \quad (15)$$

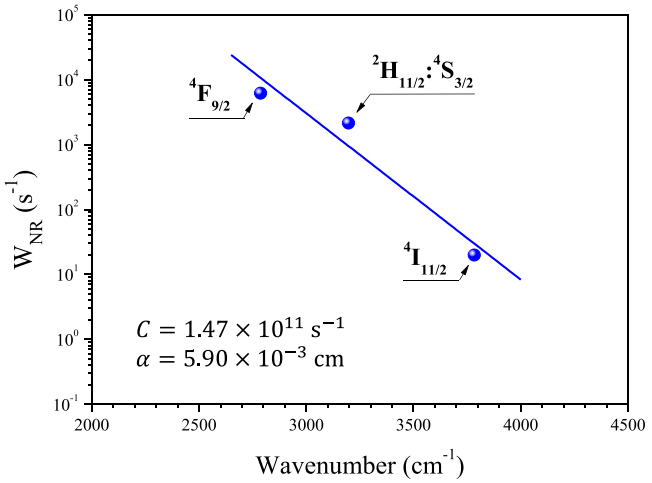

Fig. 11. Non-radiative transition probabilities as function of the energy difference between the two levels involved in the transition. Solid line represents the linear fit to Eq. (15).

where C and α are positive constants which depend only on the particular host.

Fig. 11 depicts the non-radiative transition probabilities of $^4F_{9/2}$, $^2H_{11/2}$:$^4S_{3/2}$ and $^4I_{11/2}$ levels in CaF_2: Er^{3+} NPs as function of the energy gap. As it can be appreciated, the non-radiative transition probabilities can be perfectly fitted to Eq.(14) considering that the constants in the gap law are $C = 1.47 \times 10^{11}$ s^{-1} and $\alpha = 5.90 \times 10^{-3}$ cm. This gap law stablishes that the non-radiative transition probability for the $^4I_{13/2}$ level ($\Delta E \sim 6540$cm^{-1}) is around $W_{NR} = 4.4 \times 10^{-6}$ s^{-1}, value that can be effectively neglected compared to its raditive transition probability ($A_{rad} = 100$s^{-1}). Additionally, in the case of the intermediate $^4I_{9/2}$ level ($\Delta E \sim 2280$cm^{-1}), the gap law indicates that its non-raditive decay rate ($W_{NR} = 2.1 \times 10^5$ s^{-1}) is much higher that the radiative one ($A_{rad} = 96$s^{-1}), which is in perfect accordance with the absence of radiative transitions from this level in the emission spectra independently on the excitation wavelength.

4. Conclusions

In this work, CaF_2:Er^{3+} NPs were synthesized by a direct precipitation method. The crystalline structure and morphology have been investigated as function of the erbium content. The results indicate that, within the concentration range explored in this work, the NPs structure is compatible with the fluoride-type structure exhibiting the cubic morphology typical of the CaF_2 crystals. The Rietveld refinement indicates that the unit cell volume increases monotonously from 162.92 (Å)^3 to 163.70 (Å)^3 when erbium concentration increases from 0 mol% to 10 mol%.

The photoluminescent characterization has been performed under CW and pulsed excitation. The CW excitation at $\lambda = 488$nm give rise to the occurrence of several emission bands corresponding to the $^2H_{11/2}$:$^4S_{3/2} \rightarrow {}^4I_{15/2}$, $^4F_{9/2} \rightarrow {}^4I_{15/2}$, $^2H_{11/2}$:$^4S_{3/2} \rightarrow {}^4I_{13/2}$, $^4I_{11/2} \rightarrow {}^4I_{15/2}$ and $^4I_{13/2} \rightarrow {}^4I_{15/2}$ erbium transitions. The study reveals that all of these transitions are affected by luminescence quenching processes when [Er^{3+}] ≥ 3.8 mol%. It has been found that the critical concentration for this kind of processes is located around $N_C = 5.2$mol%, value at which the luminescence quantum efficiency is reduced till $\eta = 50\%$.

The dynamics of the emitting manifolds has been investigated under pulsed excitation. The luminescent decays have been characterized in terms of an effective decay time. The dependence of these decay times on the dopant level can be understood by considering the simuoltaneous presence of luminescence quenching and radiation trapping processes. A treatment, commonly used in bulk doped materials, has been applied to determine the intrinsic total transition probabilities of $^4I_{13/2}$, $^4I_{11/2}$, $^4F_{9/2}$ and $^2H_{11/2}$:$^4S_{3/2}$ levels in absence of quenching and radiation trapping.

The intrinsic total transition probability of $^4I_{13/2}$ level has been used to perform a modified Judd-Ofelt analysis. The radiative transition probabilities, radiative lifetimes and branching ratios have been calculated using the obtained intensity parameters: $\Omega_{2,4,6}$=1.97, 0.91 and 1.34, in units of 10^{-20} cm^2. Finally, the gap law in these NPs has been estimated.

Data availability

The data that has been used is confidential.

Declaration of Competing Interest

The authors declare the following financial interests/personal relationships which may be considered as potential competing interests: Eugenio Cantelar reports financial support was provided by Ministerio de Ciencia e Innovación (Spain).

Acknowledgements

This work has been partially supported by Ministerio de Ciencia e Innovación (Spain) under project COLUMNAS (PID2019–110632RB-I00).

Appendix A. Supporting information

Supplementary data associated with this article can be found in the online version at doi:10.1016/j.jallcom.2023.170192.

References

[1] A. Nsubuga, M. Sgarzi, K. Zarschler, M. Kubeil, R. Hübner, R. Steudtner, B. Graham, T. Joshi, H. Stephan, Facile preparation of multifunctionalisable 'stealth' upconverting nanoparticles for biomedical applications, Dalton Trans. 47 (2018) 8595.
[2] C.D.S. Brites, E.D. Martínez, R.R. Urbano, C. Rettori, L.D. Carlos, Self-calibrated double luminescent thermometers through upconverting nanoparticles, Nanoparticles, Front. Chem. 7 (2019) 267.
[3] L. Francés-Soriano, N. Peruffo, M.M. Natile, N. Hildebrandt, Er^{3+}-to-dye energy transfer in DNA-coated core and core/shell/shell upconverting nanoparticles with 980 nm and 808 nm excitation of Yb^{3+} and Nd^{3+}, Analyst 145 (2020) 2543–2553.
[4] S. Wen, J. Zhou, K. Zheng, A. Bednarkiewicz, X. Liu, D. Jin, Advances in highly doped upconversion nanoparticles, Nat. Commun. 9 (2018) 2415.
[5] B. Chen, F. Wang, Combating concentration quenching in upconversion nanoparticles, Acc. Chem. Res. 53 (2020) 358–367.
[6] F. Pini, L. Francés-Soriano, N. Peruffo, A. Barbon, N. Hildebrandt, M.M. Natile, Spatial and temporal resolution of luminescence quenching in small upconversion nanoparticles, ACS Appl. Mater. Interfaces 14 (2022) 11883–11894.
[7] A.I. Becerro, D. González-Mancebo, E. Cantelar, F. Cussó, G. Stepien, J.M. de la Fuente, M. Ocaña, Ligand-free synthesis of tunable size Ln:BaGdF5 (Ln = Eu^{3+} and Nd_{3+}) nanoparticles: luminescence, magnetic properties, and biocompatibility, Langmuir 32 (2016) 411–420.
[8] F. Auzel, G. Baldacchini, L. Laversenne, G. Boulon, Radiation trapping and self-quenching analysis in Yb3+, Er3+ and Ho3+ doped Y2O3, Opt. Mat. 24 (2003) 103–109.
[9] P. Villanueva-Delgado, K.W. Krämer, R. Valiente, Simulating energy transfer and upconversion in β-NaYF4:Yb3+,Tm3+, J. Chem. Phys. C 119 (2015) 23648–23657.
[10] J. Tu, S.A. FitzGerald, J.A. Campbell, A.J. Sievers, Glass-like properties observed in low frequency Raman scattering of mixed fluoride crystals, J. Non-Cryst. Solids 203 (1996) 153–158.
[11] J. Corish, C.R.A. Catlow, P.W.M. Jacobs, S.H. Ong, Defect aggregation in anion-excess fluorites, Dopant Monomers dimers, Phys. Rev. B 25 (1982) 6425–6438.
[12] T.P.J. Han, G.D. Jones, R.W.G. Syme, Site-selective spectroscopy of Nd^{3+} centers in CaF_2:Nd^{3+} and SrF_2:Nd^{3+}, Phys. Rev. B 47 (1993) 14706–14723.
[13] V. Petit, P. Camy, J.-L. Doualan, X. Portier, R. Moncorgé, Spectroscopy of Yb3+:CaF2: from isolated centers to clusters, Phys. Rev. B 78 (2008) 085131.
[14] F. d'Acapito, S. Pelli-Cresi, W. Blanc, M. Benabdesselam, F. Mady, P. Gredin, M. Mortier, J. Phys.: Condens. Matter 28 (2016) 485301.
[15] T. Som, B. Karmakar, Efficient green and red fluorescence upconversion in erbium doped new low phonon antimony glasses, Opt. Mater. 31 (2009) 609–618.

[16] L. Guo, Y. Wang, Z. Zou, B. Wang, X. Guo, L. Han, W. Zeng, Facile synthesis and enhancement upconversion luminescence of ErF_3, nano/Microstruct. via Li^+ doping, J. Mater. Chem. C. 2 (2014) 2765.
[17] D. Avram, I. Tiseanu, B.S. Vasile, M. Florea, C. Tiseanu, Near infrared emission properties of Er doped cubis sesquioxides in the second/third biological windows, Sci. Rep. 8 (2018) 18033.
[18] E.E. Brown, Z.D. Fleischman, J. McKay, M. Dubinskii, Spectroscopic characterization of low-phonon Er-doped BaF_2 single crystal for mid-IR lasers, Opt. Mater. Express 11 (2021) 575–584.
[19] E. Cantelar, G. Lifante, L. Grima, J.I. Peña, D. Sola, Quantification of the resonant energy transfer processes in Er^{3+}/Yb^{3+} co-doped $Ca_3Al_2Si_3O_{12}$ glasses, J. Lumin. 253 (2023) 119484.
[20] A. Bensalah, M. Mortier, G. Patriarche, P. Gredin, D. Vivien, Synthesis and optical characterizacion of undoped and rare-earth doped CaF_2 nanoparticles, J. Solid State Chem. 179 (2006) 2636–2644.
[21] G.A. Kumar, C.W. Chen, R.E. Riman, Optical spectroscopy and confocal luminescence imagin of upconverting Er^{3+}-doped CaF_2 nanocrystals, Appl. Phys. Lett. 90 (2007) 093123.
[22] G. Zhi, J. Song, B. Mei, W. Zhou, Synthesis and characterization of Er^{3+} doped CaF_2, Nanopart., J. Alloy. Compd. 509 (2011) 9133–9137.
[23] A. Lyapin, P.A. Ryabochkina, S.V. Gushchin, M.N. Zharkov, A.S. Ermakov, V.M. Kyashkin, S.V. Peytkov, A.V. Atanova, Characteristics of upconversion luminescence of CaF_2:Er powders excited by 1.5-μm laser radiation, Opt. Spectrosc. 128 (2020) 200–206.
[24] F. Wang, X. Fan, D. Pi, M. Wang, Synthesis and luminescence behavior of Eu^{3+}-doped CaF_2 nanoparticles, Solid State Commun. 133 (2005) 775–779.
[25] W. Ye, X. Liu, Q. Huang, Z. Zhou, G. Hu, Eu^{2+} nanoparticles using different surfactants, Mat. Res. Bull 83 Co-precipitation synthesis and self-reduction of CaF2,, 2016, pp. 428–433.
[26] E. Cantelar, J.A. Sanz-García, A. Sanz-Martín, J.E. Muñoz Santiuste, F. Cussó, Structural, photoluminescent properties and Judd-Ofelt analysis of Eu^{3+} activated CaF_2, Nanocubes, J. Alloy. Compd. 813 (2020) 152194.
[27] R. Wang, M. Yuan, C. Zhang, H. Wang, X. Xu, Tunable multicolor and enhanced red emission of monodispersed CaF2:Yb3+/Ho3+ microspheres via Mn2+ doping, Opt. Mat. 79 (2018) 403–407.
[28] A.B. Andrade, N.S. Ferreira, M.E.G. Valerio, Particle size effects on structural and optical properties of BaF_2 nanoparticles, RSC Adv. 7 (2017) 26839–26848.
[29] A. Zamkovskaya, E. Maksimova, I. Nauhatsky, Size-strain line-broadening analysis of the calcite-type borate ABO_3 (A = Fe, In, Ga,), J. Phys. Conf. Ser. 1135 (2018) 012020.
[30] Z. Chouahda, J.P. Jouart, T. Duvaut, M. Diaf, The use of green emission in Er^{3+}-doped CaF_2, Cryst. Thermom. Appl., J. Phys.: Condens. Matter 21 (2009) 245504.
[31] M. Quintanilla, E. Cantelar, F. Cussó, M. Villegas, A.C. Caballero, Temperature sensing with up-converting submicron-sized $LiNbO_3$:Er^{3+}/Yb^{3+} particles, Appl. Phys. Express 4 (2011) 022601.
[32] S. Zhou, K. Deng, X. Wei, G. Jiang, C. Duan, Y. Chen, M. Yin, Upconversion luminescence of $NaYF_4$:Yb^{3+},Er^{3+} for temperature sensing, Opt. Commun. 291 (2013) 138–142.
[33] F. Huang, Y. Gao, J. Zhou, J. Xu, Y. Wang, Yb^{3+}/Er^{3+} co-doped $CaMoO_4$: a promising green up-conversion phosphor for optical temperature sensing, J. Alloy. Comp. 639 (2015) 325–329.
[34] S. Rohani, M. Quintanilla, S. Tuccio, F. De Angelis, E. Cantelar, A.O. Govorov, L. Razzari, F. Vetrone, Enhanced luminescence, collective heating, and nanothermometry in an ensemble system composed of lanthanide-doped upconverting nanoparticles and gold nanorods, Adv. Optical, Mater 3 (2015) 1606–1613.
[35] Y. Hua, J.S. Yu, Strong green emission of erbium(III)-activated La_2MgTiO_6 phosphors for solid-state lighting and optical temperature sensors, ACS Sustain. Chem. Eng. 9 (2021) 5105–5115.
[36] N.O. Nuñez, F. Cussó, E. Cantelar, B. Martin-Garcia, J.M. de la Fuente, A. Corral, M. Balcerzyk, M. Ocaña, Bimodal Nd-doped $LuVO_4$ nanoprobes functionalized with polyacrilic acid for X-Ray computed tomography and NIR luminescent imaging, Nanomaterials 10 (2020) 149.
[37] D.L. Dexter, J.H. Schulman, Theory Conc. quenching Inorg. phosphors, J. Chem. Phys. 22 (1954) 1063–1070.
[38] D.F. de Sousa, L.A.O. Nunes, Microscopic and macroscopic parameters of energy transfer between Tm^{3+} ions in fluoroindogallate glasses, Phys. Rev. B 66 (2002) 024207.
[39] C. Labbé, J.L. Doualan, R. Moncorgé, A. Braud, P. Camy, Excited-state absorption and fluorescence dynamics in Er:CaF_2, J. Lumin. 200 (2018) 74–80.
[40] B.R. Judd, Optical absorption intensities of rare-earth ions, Phys. Rev. 127 (1962) 750–761.
[41] G.S. Ofelt, Intensities, Cryst. Spectra rare-earth ions, J. Chem. Phys. 37 (1962) 511–520.
[42] E. Cantelar, M. Marin-Dobrincic, T. Jardiel, A.C. Caballero, F. Cussó, Judd-Ofelt analysis of powder samples: LiNbO3:Er3+ submicron-sized particles as a model case, Opt. Mat. 41 (2015) 122–125.
[43] A. Egaña, M. Tardío, C. de la Torre-Gamarra, A. Várez, E. Cantelar, J.E. Santiuste, J. Lumin, 202 (2018) 232–238.
[44] W.T. Carnall, H. Crosswhite, H.M. Crosswhite, Energy level structure and transition probabilities in the spectra of the trivalent lanthanides in LaF_3, Argonne Natl. Lab (1978).
[45] I.H. Malitson, A redetermination of some optical properties of calcium fluoride, Appl. Opt. 2 (1963) 1103–1107.
[46] G. Buse, E. Preda, M. Stef, A. Pruna, F. Stef, I. Nicorana, Judd-Ofelt analysis of the Er3+ ions in double-doped CaF2:(Er3+, Yb3+) crystal, AIP Conference Proceedings 1131 (2009) 131–135.
[47] R. Xing, B. Mei, J. Song, X. Li, Fluorescence and Judd-Ofelt analysis of Er^{3+} doped CaF_2 transparent ceramic, Adv. Mater. Res. 875- 877 (2014) 23–27.